RSC Advances

PAPER

View Article Online
View Journal | View Issue

Cite this: *RSC Adv.*, 2024, **14**, 27465

A flexible solid-state asymmetric supercapacitor device comprising cobalt hydroxide and biomass-derived porous carbon†

Rajeshvari Samatbhai Karmur,‡[a] Debika Gogoi,‡[a] Manash R. Das[bc] and Narendra Nath Ghosh*[a]

Development in the field of alternative and renewable energy sources is becoming necessary considering the current energy demands of the growing technologies. The main challenge associated with the produced energy is to store it for future use, such that it can be used when needed. Supercapacitors are among the electrochemical energy storage systems that provides higher power density, faster charging–discharging, high specific capacitance (C_S), and long cycling life. Herein, the fabrication of a flexible solid-state asymmetric supercapacitor (ASC) device is reported, where $Co(OH)_2$ hollow spheres and biomass-derived porous carbon (PC) are the cathode and anode, respectively. $Co(OH)_2$ is a highly redox active material, whereas PC is an electric double-layer capacitive (EDLC) material. In this device, aqueous KOH solution (electrolyte) encapsulated in PVA gel (separator) was used to bind the electrodes. This $Co(OH)_2$//PC ASC device exhibited a high C_S of 260 F g^{-1} (at 2 A g^{-1}). It retained ~91% of the initial C_S value (at 6 A g^{-1}) till ~5000 cycles. Electrochemical impedance spectroscopy (EIS) study confirmed low internal resistance (0.95 Ω) and charge transfer resistance (1.41 Ω) values of $Co(OH)_2$//PC. These results indicate that the high electron transfer process in the electrode–electrolyte interface during the electrochemical reaction, which is responsible for the excellent performance of this ASC device. The high-performance $Co(OH)_2$//PC ASC device exhibited an energy density of 76.7 W h kg^{-1} at a power density of 1416.9 W kg^{-1}. To demonstrate its practical use, LED lights were illuminated using this $Co(OH)_2$//PC ASC device.

Received 15th July 2024
Accepted 18th August 2024

DOI: 10.1039/d4ra05106h

rsc.li/rsc-advances

1. Introduction

The world is now implementing a low-emission development strategy.[1,2] This strategy mainly focuses on the security of forests, the environment, and climate change. The decline in long-term greenhouse gas emissions and improved resilience to climate change could be effective measures for this implementation. This leads to a transition from the use of fossil fuels to renewable and sustainable energy conversion and storage technologies.[3] The important role of energy storage and conversion devices is to store electricity during spare time at a low cost and deliver it later. Among the various developed electrochemical energy storage technologies (batteries, capacitors, fuel cells, supercapacitors, *etc.*),[4,5] supercapacitors have attracted widespread attention from researchers. Supercapacitors can quickly store and deliver energy by offering higher current in a short time than batteries and exhibit higher energy density in comparison to traditional capacitors, which enables them to provide high power density and moderate energy density to bridge the gap between both batteries and parallel plate capacitors.[5–7] Supercapacitors are mainly used in many fields, such as portable electronics, electric or hybrid vehicles, uninterruptible power supplies, heavy loading trucks, cranes, and military (*i.e.*, laser weapons and missile launch systems).[8] The advance of supercapacitors primarily depends on synthesized electrode materials, their charge storage mechanism (capacitive or diffusive), electrolytes, binders, and separators. Further, supercapacitors can be divided into two categories: (i) symmetric supercapacitors and (ii) asymmetric supercapacitors (ASCs). By preparing the anode and cathode using the same material with the same mass loading, a symmetric supercapacitor device can be fabricated. Symmetric supercapacitor devices deliver a lower energy density because of their smaller voltage window, which limits their use in practical applications.[8,9] One way to enhance the energy density of a supercapacitor can be an assembly of asymmetric supercapacitor (ASC) devices using two different materials to prepare

[a]*Nano-materials Lab, Department of Chemistry, BITS-Pilani, Goa Campus, Zuarinagar, Goa-403726, India. E-mail: naren70@yahoo.com; p20200051@goa.bits-pilani.ac.in; p20180429@goa.bits-pilani.ac.in; Fax: +91 25570339; Tel: +91 832 2580318*

[b]*Advanced Materials Group, Materials Sciences and Technology Division, CSIR-NEIST, Jorhat, Assam-785006, India. E-mail: mnshrdas@yahoo.com*

[c]*Academy of Scientific and Innovative Research (AcSIR), Ghaziabad 201002, India*

† Electronic supplementary information (ESI) available. See DOI: https://doi.org/10.1039/d4ra05106h

‡ Rajeshvari Samatbhai Karmur and Debika Gogoi contributed equally to this paper.

an anode and cathode, which increases the voltage window and, consequently, the energy density. Nevertheless, with the substantial advancement made in the development of ASC devices, increasing interest in flexible and wearable energy storage systems has led to the preparation of flexible ASC devices.

$Co(OH)_2$ is an inexpensive, earth-abundance material and possesses excellent redox activity in electrochemical reactions.[10,11] $Co(OH)_2$ has two polymorphs: α-$Co(OH)_2$ and β-$Co(OH)_2$. The α-$Co(OH)_2$ structure contains intercalated molecules (*i.e.*, H_2O, NO_3) inside the interlayers, which is why it has a higher interlayer spacing than the β-$Co(OH)_2$.[12] High interlayer distance and good electronic conductivity of α-$Co(OH)_2$ deliver higher electrochemical activity compared to β-$Co(OH)_2$. However, the nanostructure of cobalt hydroxide suffers from agglomeration, poor electronic conductivity, and slow ion diffusion kinetics, which can lead to a low reversible capacity when used as high-performance electrodes.[13,14] Different morphologies of the metal hydroxides show different electrochemical activities.[15,16] Innovative nanostructures, such as hollow, core–shell, and hollow–core–shell designs, must be explored to achieve enhanced electrochemical performance because of their high surface-to-volume ratios, large surface areas, excellent permeabilities, and abundant surface-active sites. These attributes are crucial for achieving high energy and power densities in electrochemical supercapacitors.[13] For instance, utilizing nanospheres instead of nanosheets can significantly increase the material's specific surface area and reduce the "dead volume" that occurs when internal sheet materials are unable to interact with the external environment due to accumulation.[17]

In this work, a hollow sphere-like structure formed by a combination of flakes of $Co(OH)_2$ was synthesized to develop a solid-state asymmetric supercapacitor (ASC) device. Besides, biomass-derived porous carbon was synthesized using tea waste (after brewing the tea leaves) as precursors. The $Co(OH)_2$ showed pseudocapacitive redox activity and was utilized as cathode material, and the EDLC behavior of PC established its role as anode material for the fabrication of the ASC device. The anode material of the ASC device also plays an important role. Another key component in the equipped device was the use of polymeric gel to act as a solid-state electrolyte, which made the device flexible. In particular, aqueous gel electrolytes are the most studied because they combine the advantages of both aqueous and solid electrolytes.[18,19] Here, polyvinyl alcohol (PVA) was selected to entrench a 3 M KOH aqueous electrolyte into a gel because of its high solubility in water, low toxicity, and low cost. The electrochemical performances of a flexible solid-state $Co(OH)_2$//PC ASC device were examined using a two-electrode system (2E-cell), and parameters such as specific capacitance (C_S) value, energy and power densities, flexibility, and stability were calculated. The device exhibited a high C_S value of 260 F g^{-1} at a current density of 2 A g^{-1}. It delivered a higher energy density of 76.7 W h kg^{-1} at a power density of 1416.9 W kg^{-1}, which is comparable to and superior to many already reported $Co(OH)_2$-based asymmetric supercapacitor devices.[12,20–23] The cyclic stability of the device after ∼5000 galvanostatic charge–discharge (GCD) cycles was 91% observed. A series of 16 red LEDs were illuminated with the prepared solid-state ASC device. The present work elaborates on the successful synthesis of the nanomaterials and nanocomposites, the excellent electrochemical activity of synthesized materials, the assembly of a solid-state ASC device, the high performance of the assembled device, its flexibility, stability, and its practical application on a lab scale demonstration.

2 Experimental

2.1 Synthesis of materials

2.1.1 Synthesis of the cathode material ($Co(OH)_2$). A hollow-sphere structured $Co(OH)_2$ was synthesized using a one-step hydrothermal process. First, 4 mM of $Co(NO_3)_2 \cdot 6H_2O$ in 30 mL of ethanol and 8 mM of urea in 30 mL of ethanol were mixed together. Then, 12 mg of trisodium citrate ($Na_3C_6H_5O_7$) was added to the prepared solution and stirred for 30 min. After that, the clear solution was transferred to a Teflon-lined stainless steel autoclave and heated at 150 °C for 24 h. The brown precipitate of $Co(OH)_2$ was obtained after centrifugation, washed repeatedly, and dried at 60 °C.

2.1.2 Preparation of the anode using porous carbon derived from tea waste. Porous carbon was synthesized from a bio-mass (tea waste) using the KOH activation method. In the first step, 2 gm of tea waste was treated with 50 mL of conc. H_2SO_4 at 200 °C for 24 h. Then, the obtained black product (precursor) was washed with distilled water and then dried. In the second step, the precursor was mixed with an equivalent amount of KOH and then calcined at 900 °C for 3 h in a nitrogen atmosphere. Then, it was washed with distilled water and dried for further use, and the obtained product was porous carbon (PC).[24]

2.2 Electrochemical measurements

2.2.1 Three-electrode cell setup and measurements. Three-electrode cell (3E-cell) configuration was used to study the electrochemical properties of synthesized $Co(OH)_2$ and PC. The Hg/HgO electrode was used as a reference electrode, and a Pt wire was used as a counter electrode. The working electrode was fabricated by preparing a slurry of synthesized material, PVDF in NMP, and acetylene black in a ratio of 80 : 10 : 10. A paste was coated on a Ni foam with a mass of ∼2 mg. From this 3E-cell setup, important parameters of the electrode materials, such as capacitance, voltage window, and charge transfer resistance, were measured by employing cyclic voltammetry (CV), galvanostatic charge–discharge (GCD), and electrochemical impedance spectroscopy (EIS) tests. EIS measurements were conducted in the frequency range of 0.01–10000 Hz with an alternating current amplitude of 0.05 V.

2.2.2. Two-electrode cell setup (asymmetric supercapacitor device) and measurements. An asymmetric cell was assembled with $Co(OH)_2$ (cathode) and PC (anode), Whatman filter paper as a separator, and 3 M KOH as an electrolyte. The cathode-to-anode mass ratio was determined from the charge balance equation (eqn S6†) ($m^+/m^- = 1.28$). Here, the cathode was prepared using ∼1.56 mg of $Co(OH)_2$, and for the anode, ∼2 mg

of PC was used. The operating voltage window of 0 to 1.5 V was determined from the 3E-cell measurements of the cathode and anode. A solid-state supercapacitor device was constructed using the same cathode and anode materials as the asymmetric cell. In this case, a polymer gel (PVA) containing 3 M KOH was used, which acted as both a separator and an electrolyte. All the equations used to calculate the different parameters of the supercapacitor device are presented in the ESI.†

3 Results and discussion

3.1 Structural and morphological analysis

Fig. 1a presents a powder XRD pattern of $Co(OH)_2$, in which the diffraction peaks at 2θ values of 11.1, 22.2, 33.4, 37.7, and 59.5° corresponding to (003), (006), (100), (102), and (110) planes were observed [JCPDS card no.: 46-0605]. The (003) plane obtained *d*-values of 8.03 Å and showed higher intensity than other planes, which suggested that the α-$Co(OH)_2$ was formed with a greater number of interlayer spacers, such as H_2O and NO_3^-, and a more ordered structure in the direction of the (003) plane.[25] XRD pattern of porous carbon showed an amorphous nature with two humps between 2θ values of 21–34 and 39–48° (Fig. 1b).[24]

Raman spectroscopy analysis of the $Co(OH)_2$ is displayed in Fig. 1c. The spectra showed two vibrational bands at 450 and 510 cm^{-1}, corresponding to A_{1g} and A_{2u}, respectively. The observed Raman shift at 450 cm^{-1} was due to the OCoO vibrational mode.[26,27] An intense peak was observed at 510 cm^{-1}, which was assigned to the Co–O–H mode.[28] Fourier transform infrared spectroscopy (FTIR) of $Co(OH)_2$ is presented in Fig. 1d. The bands at 3615, 1480, 1382, 1352, 1050, and 640 cm^{-1} were obtained. A broad peak observed at 3615 cm^{-1} corresponds to the stretching vibration of the O–H groups.[29] A sharp peak appeared at 1382 cm^{-1}, which was the characteristic peak of nitro groups and indicated the presence of intercalated NO_3^- ions in the cobalt hydroxide.[30,31] The peaks appearing at 1480, 1352, and 1050 cm^{-1} were ascribed to the intercalated carbonate ions in the α-$Co(OH)_2$.[30,32] A peak observed at 640 cm^{-1} was assigned to Co–O–H vibration.[31]

A field emission scanning electron microscopy (FESEM) study showed a hollow sphere-like morphology of the synthesized $Co(OH)_2$ within the diameter of 7–9 μm (Fig. 2a). The magnified image of the $Co(OH)_2$ hollow sphere depicted its hollowness (Fig. 2b), which was formed due to the assemblage of ~0.22 μm long petals. The elemental color mapping of $Co(OH)_2$ displayed the presence of Co and O, as shown in Fig. 2c–e. The energy dispersive X-ray spectroscopy (EDS) study of the $Co(OH)_2$ is shown in Fig. S1,† in which the Co and O were observed. A highly porous matrix was observed in the FESEM micrograph of the synthesized PC, and it is presented in Fig. 2f. High-resolution transmission electron microscopy (HRTEM) presented in Fig. 2g shows the structural features of $Co(OH)_2$ in more detail. The lattice fringe spacings of 0.38, 0.23, and 0.19 nm attributed to the (006), (105), and (108) planes of $Co(OH)_2$ were observed in the HRTEM micrograph (Fig. 2h) [JCPDS card no.: 46-0605].[33,34] The selected area electron diffraction (SAED) pattern of the $Co(OH)_2$ hollow-sphere showed well-ordered diffraction rings corresponding to (006), (100), (105), and (110) planes (Fig. 2i), which coincide with XRD pattern and also confirmed its polycrystalline structure.

X-ray photoelectron spectroscopy (XPS) analysis of the $Co(OH)_2$ was carried out to assess the chemical states of the elements. The XPS survey spectrum of the $Co(OH)_2$ is shown in Fig. 3a, which indicates the peak appearance of Co 2p and O 1s at binding energies of 531 and 782 eV, respectively. The high-

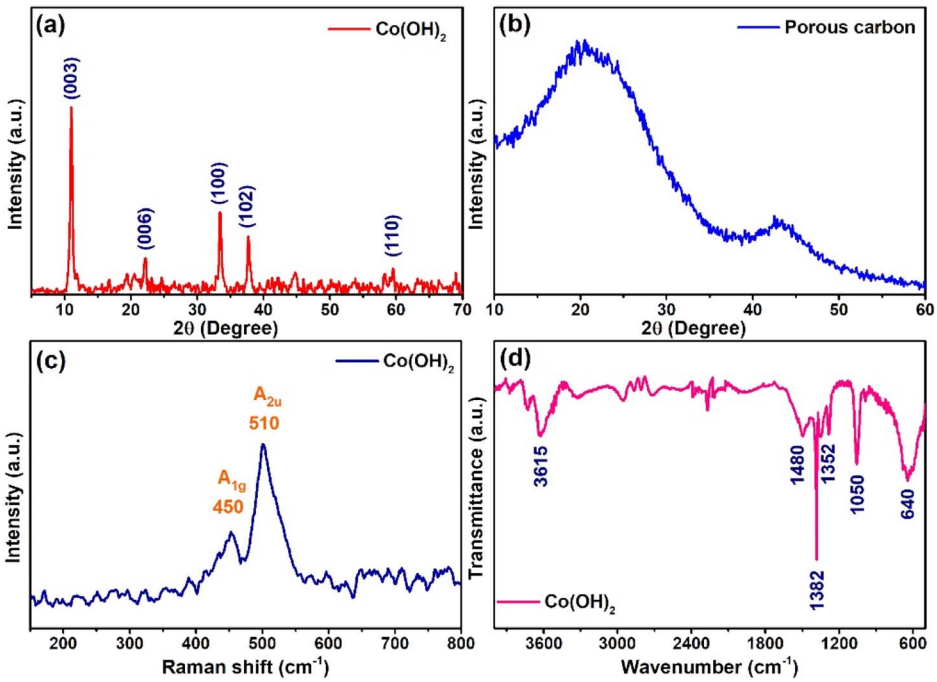

Fig. 1 XRD pattern of (a) $Co(OH)_2$ and (b) porous carbon. (c) Raman spectra and (d) FTIR spectra of $Co(OH)_2$.

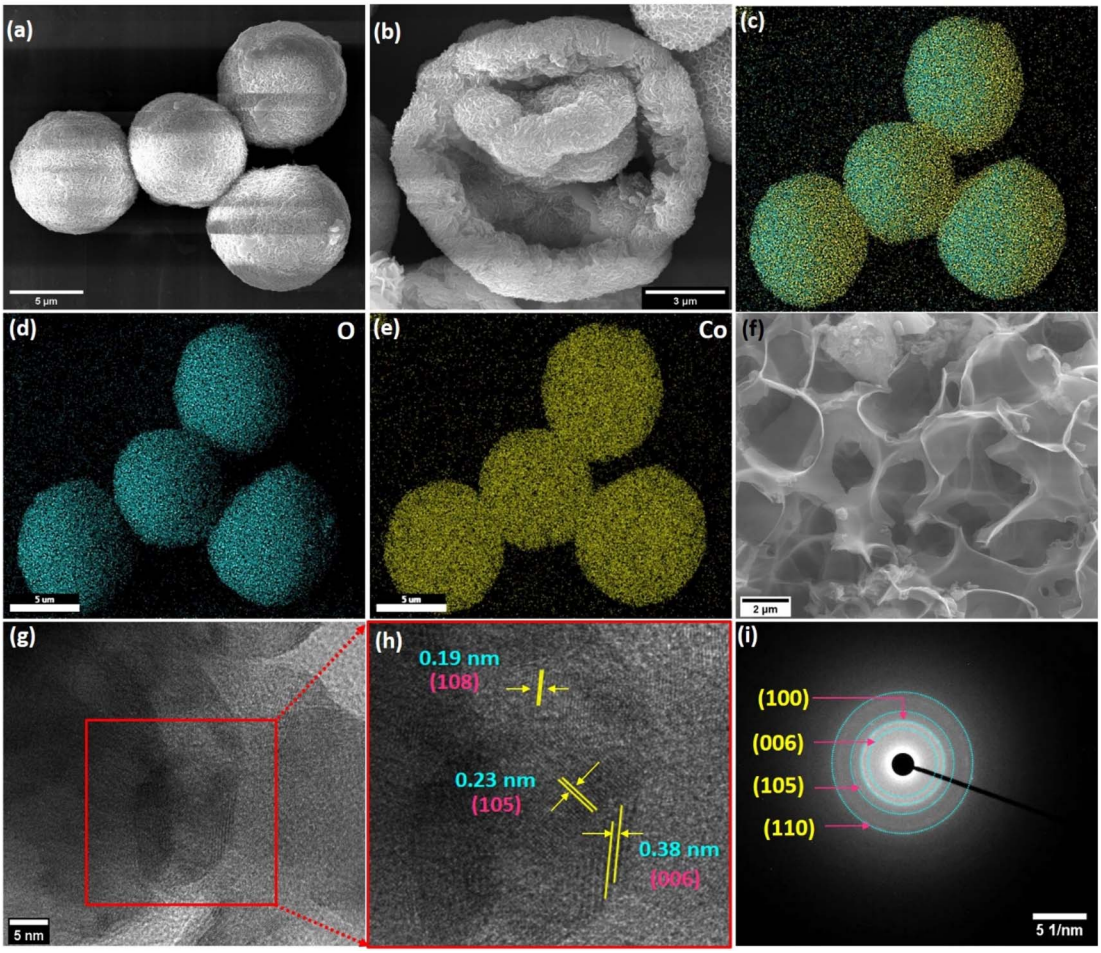

Fig. 2 (a and b) FESEM images of $Co(OH)_2$. EDS elemental color mapping of $Co(OH)_2$: (c) overlay, (d) O, and (e) Co. (f) FESEM image of porous carbon. (g and h) HRTEM images and (i) SAED pattern of $Co(OH)_2$.

resolution Co 2p spectrum (Fig. 3b) was fitted with two main peaks corresponding to spin–orbit doublets of Co $2p_{3/2}$ (781.07 eV), Co $2p_{1/2}$ (796.7 eV), and their satellite (sat) peaks (785.6 and 802.9 eV), which confirmed the presence of Co^{2+} state.[35,36] The O 1s spectrum was deconvoluted to two peaks at binding energies of 530.8 and 532.26 eV (Fig. 3c), assigning to metal–oxygen bond and oxygen-containing functional groups, respectively.[36]

The results from XRD, Raman, FTIR, FESEM, EDS, HRTEM, SAED, and XPS analyses confirmed the formation of $Co(OH)_2$ and PC. Scheme 1 demonstrates the preparation route of the $Co(OH)_2$ and porous carbon. The $Co(OH)_2$ preparation could have plausibly followed the three reaction steps during the hydrothermal process as hydrolysis of urea (eqn (1)), formation of Co(II)-citrate complex (eqn (2)), and nucleation of flowerlike $Co(OH)_2$ *via* substitution of $[Co_2(C_6H_4O_7)_2]^{4-}$ complex (eqn (3)).[37,38]

$$NH_2CONH_2 + 3H_2O \rightarrow 2NH_4^+ + OH^- + HCO_3^- \quad (1)$$

$$Co^{2+} + \text{citrate} \rightarrow [Co_2(C_6H_4O_7)_2]^{4-} \quad (2)$$

$$[Co_2(C_6H_4O_7)_2]^{4-} + OH^- \rightarrow Co(OH)_2 \quad (3)$$

The detailed formation protocol for the PC is elucidated in our previous work.[24] Briefly, during the reaction, the carbon source (*i.e.* tea waste) first reacts with solid KOH, and intercalation of potassium occurs in the carbon matrix.[39] After washing, the removal of potassium leads to the creation of pores. Plausible reaction steps are described as eqn (4)–(8).[24]

$$2C + 6KOH \rightarrow 2K_2CO_3 + 2K + 3H_2 \quad (4)$$

$$2K_2CO_3 \rightarrow K_2O + CO_2 \quad (5)$$

$$K_2CO_3 + 2C \rightarrow 2K + 3CO \quad (6)$$

$$CO_2 + C \rightarrow 2CO \quad (7)$$

$$C + K_2O \rightarrow 2K + CO \quad (8)$$

3.2 Electrochemical property evaluation

3.2.1 Three-electrode cell study of synthesized materials. Assessment of the electrochemical properties of the prepared $Co(OH)_2$ and PC were performed by conducting CV, GCD, and

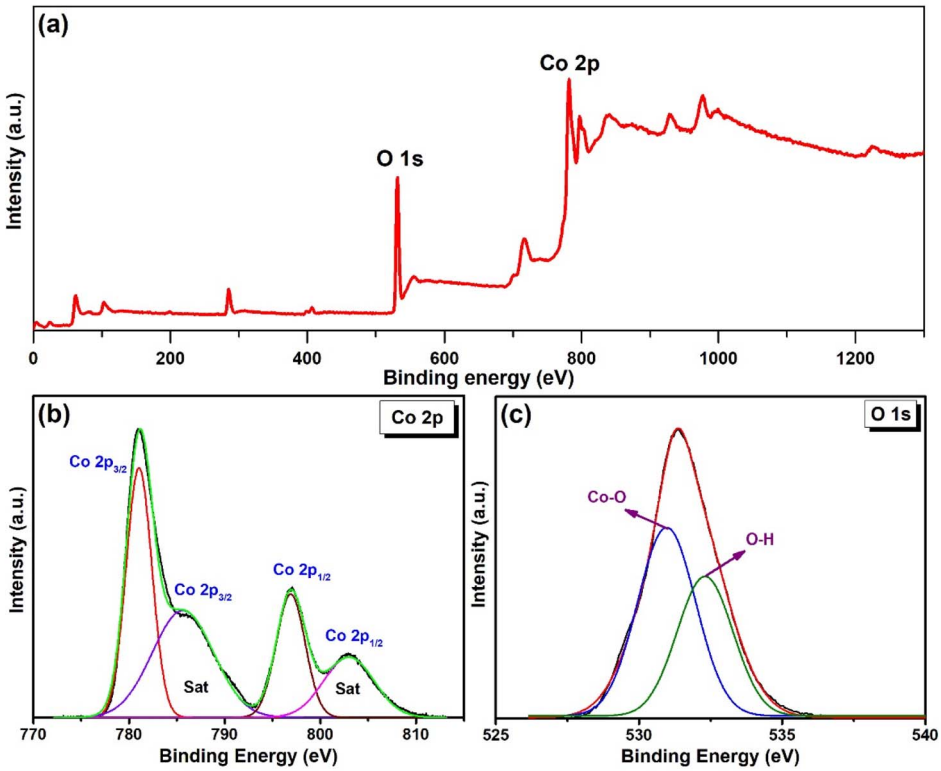

Fig. 3 XPS spectra of $Co(OH)_2$: (a) survey spectrum, (b) Co 2p, and (c) O 1s.

EIS measurements using a three-electrode (3-E) cell and 3 M KOH as the electrolyte. The working electrode was constructed by coating the active electrode materials on 1.5 cm × 1.5 cm Ni foam. A stable CV profile was achieved for $Co(OH)_2$ and PC in the potential range from 0 to 0.6 V and from −1 to 0 V, respectively. The CV profile of $Co(OH)_2$ showed two redox peaks at ~0.44/0.29 V (Fig. 4a) at a 10 mV s^{-1} scan rate, which can be attributed to its faradaic redox reactions at the electrode/electrolyte interface (eqn (9) and (10)):[40,41]

$$Co(OH)_2 + OH^- \leftrightarrow CoOOH + H_2O + e^- \quad (9)$$

$$CoOOH + OH^- \leftrightarrow CoO_2 + H_2O + e^- \quad (10)$$

When the scan rate was increased from 10 to 100 mV s^{-1}, the oxidation and reduction peaks shifted towards the forward and backward sides. These findings suggest the diffusion-controlled behavior of the redox reaction. At high scan rates, the electrode

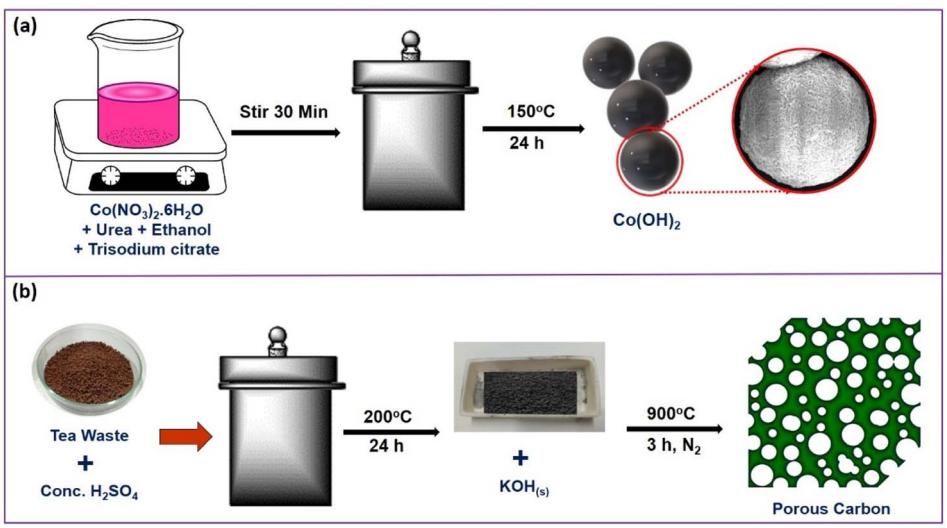

Scheme 1 Graphical illustration of the synthesis routes for (a) $Co(OH)_2$ and (b) porous carbon.

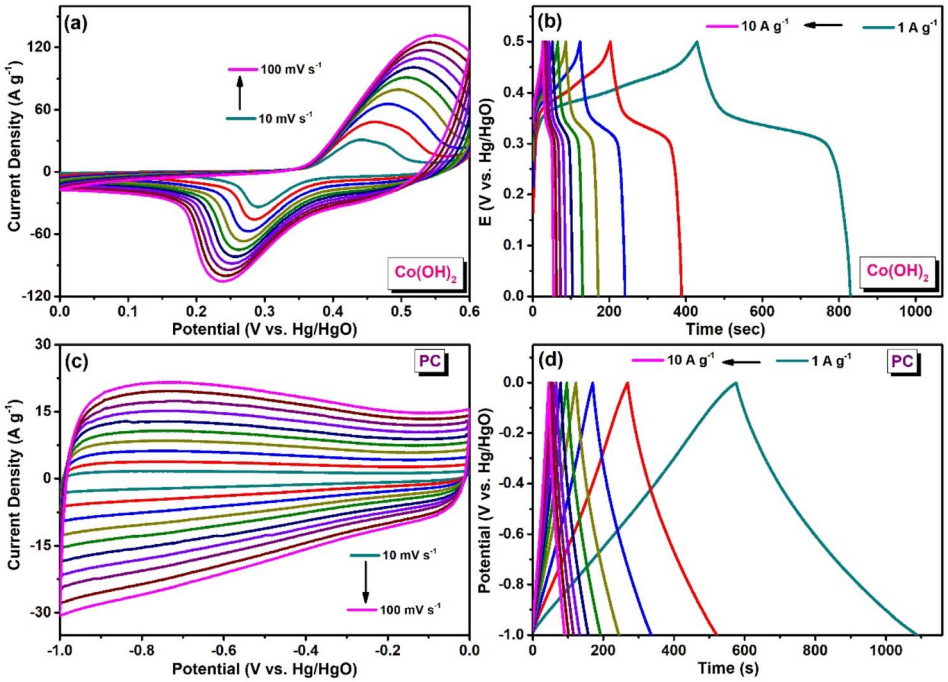

Fig. 4 (a) CV curves and (b) GCD curves of $Co(OH)_2$. (c) CV curves and (d) GCD curves of PC in 3 M KOH.

material could not efficiently access the electrolyte ions. The Randles–Sevcik plot exhibited a linear connection for the oxidation and reduction peak currents and the square root of the scan rate (Fig. S2†).

The charging and discharging properties of the $Co(OH)_2$ electrode were analyzed through galvanostatic charge–discharge (GCD) measurement (Fig. 4b). These measurements were conducted in a voltage range of 0–0.5 V. A specific capacitance value of 801 F g^{-1} at a current density of 1 A g^{-1} was attained for the $Co(OH)_2$ electrode. CV and GCD measurements of PC were performed in the potential window ranging from −1 to 0 V in 3 M KOH. Electrochemical impedance spectroscopy (EIS) of $Co(OH)_2$ was assessed in the frequency range of 0.01–10 000 Hz. Fig. S3† displays the Nyquist plot of $Co(OH)_2$. EIS measurements were performed to determine the values of charge-transfer resistance (R_{CT}) and internal resistance (R_S) of the $Co(OH)_2$ electrode in the aqueous KOH electrolyte during the electrochemical process, and a Nyquist plot was generated (Z' *vs.* Z'') (Fig. S3†). R_S and R_{CT} values were determined by fitting the data with an equivalent Randle's circuit (inset of Fig. S3†). In the Nyquist plot, the appearance of a semicircle in the high-frequency region indicates the presence of R_{CT}. R_{CT} originates from the resistance at the electrode–electrolyte interface and can be estimated from the diameter of the semicircle.[42,43] R_S signifies the combination of the ionic resistance of the electrolyte, the intrinsic resistance of the electrode material, and the contact resistance between the electrode and the current collector.[42] R_S can be determined from the intercept of the semicircle on the *x*-axis (Z') at the high-frequency region. The R_S and R_{CT} values of $Co(OH)_2$ were 0.38 and 1.98 Ω, respectively.

Fig. 4c and d present the CV and GCD of PC, respectively. The quasi-rectangular cyclic voltammogram and linear galvanostatic charging–discharging curves indicated its electric double-layer capacitive (EDLC) characteristics. PC attained a specific capacitance of 516 F g^{-1} at a current density of 1 A g^{-1}. This PC was used as the anode material in the assembled asymmetric supercapacitor (ASC) device. The highly porous structure of PC promotes rapid electrolyte ion diffusion and accelerates ion transport within the device, which could contribute to the improved performance of the device.

3.2.2 Asymmetric supercapacitor device study. A two-electrode (2-E) asymmetric cell was constructed with $Co(OH)_2$ as the cathode, tea-waste-derived PC as the anode, and a filter paper (as a separator) soaked in 3 M KOH as the electrolyte. This 2-E cell can be designated as $Co(OH)_2$//PC, and its operational potential can be extended up to 1.5 V (Fig. 5a). Beyond that potential, the CV profile showed slight distortion caused by the thermodynamic breakdown of water (Fig. 5b). Fig. 5c shows the CV profiles of the ASC cell in the potential range of 0–1.5 V, depicting good stability even at high scan rates. Besides, the ASC cell also showed stable GCD curves at different current densities (2 to 12 A g^{-1}) (Fig. 5d), which was congruous with its CV observations. These analyses indicated that the ASC cell possesses great electrochemical reversibility. At the current densities of 2 and 12 A g^{-1}, the ASC cell exhibited a C_S value of 225.3 F g^{-1} and 200 F g^{-1}, respectively. Fig. 5e presents the derived Ragone plot of the ASC cell from its energy and power densities, which demonstrated that it has the capability of supplying an energy density of 57.4 W h kg^{-1} at a power density of 1222.7 W kg^{-1}. The EIS measurements revealed that it possesses R_S and R_{CT} values of 0.6 and 1.06 Ω, respectively. The obtained Nyquist plot is presented in Fig. 5f.

The successful fabrication of the ASC cell encouraged us to construct a solid-state supercapacitor device to demonstrate the potentiality of the synthesized materials in modern portable

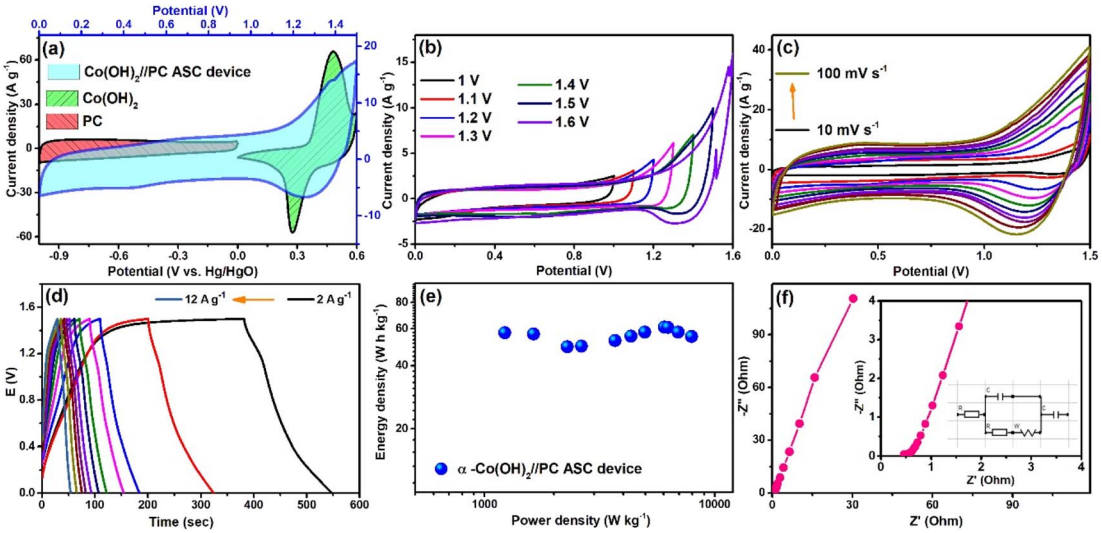

Fig. 5 (a) CV curves of $Co(OH)_2$ (0–0.6 V), PC (−1–0 V), and $Co(OH)_2$//PC ASC devices (0–1.5 V) at a scan rate of 30 mV s^{-1}. (b) CV curves with different potential window, (c) CV curves with different scan rates, (d) GCD profile with different current densities, (e) Ragone plot, and (f) Nyquist plot (inset: Nyquist plot in the high-frequency region and fitted circuit) of the $Co(OH)_2$//PC ASC device.

electronic devices. Here, both the cathode and anode were kept the same as in the previous ASC cell, but the filter paper was replaced by solidified 3 M KOH encapsulated PVA gel. In this case, PVA gel acted as the separator, and aqueous KOH was the electrolyte. This also acts as the electrolyte in the fabricated solid-state supercapacitor device. The as-constructed device is graphically portrayed in Fig. 6a. Then, to analyze the performance of the device, different parameters, such as specific capacitance (C_S), energy and power densities, and coulombic efficiency, were evaluated. Fig. 6b presents the CV curves of this device at scan rates varying from 10 to 100 mV s^{-1}, which displays the retention of the initial shape with the increase in scan rates. This depicted the occurrence of reversible electrochemical processes in the device. The GCD curves of the device measured at numerous current densities are shown in Fig. 6c, and the observed C_S value at 2 A g^{-1} was 260 F g^{-1}. The device also exhibited a coulombic efficiency of ~100% (Fig. S4†) at 6 A g^{-1}; hence, a stability test was conducted at this current density. After ~5000 cycles of constant charging and discharging processes, the device retained ~91% of its initial C_S value, demonstrating a long lasting shelf life (Fig. 6d). Fig. S5† displays the XRD and FESEM analyses of the $Co(OH)_2$. After ~5000 GCD cycles, no significant changes were observed in the structural properties and morphology of the electrode material.

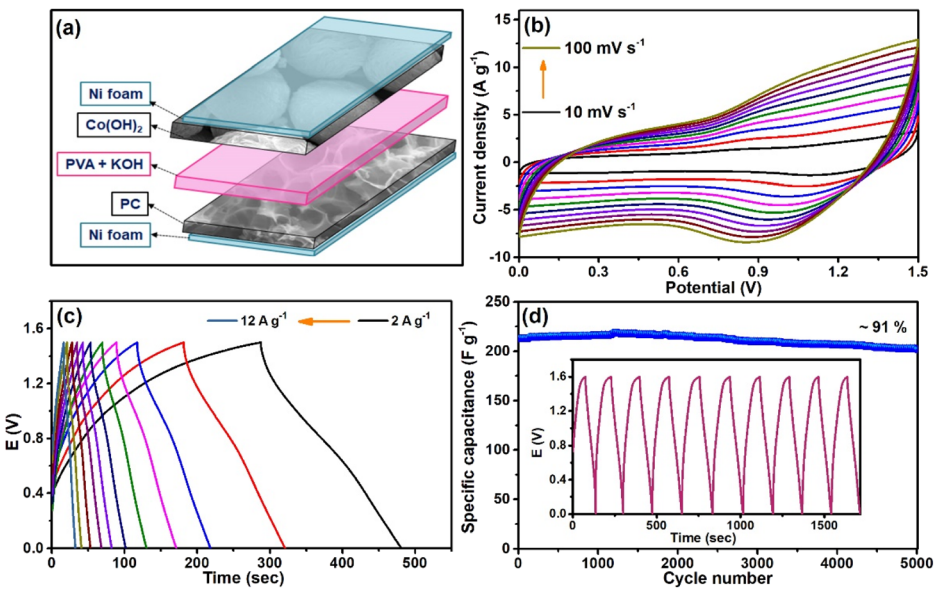

Fig. 6 (a) Graphical sketch of a solid-state $Co(OH)_2$//PC ASC device. (b) CV scans and (c) GCD curves of the solid-state $Co(OH)_2$//PC ASC device. (d) Cycling stability test (inset: first GCD 10 cycles) of the device.

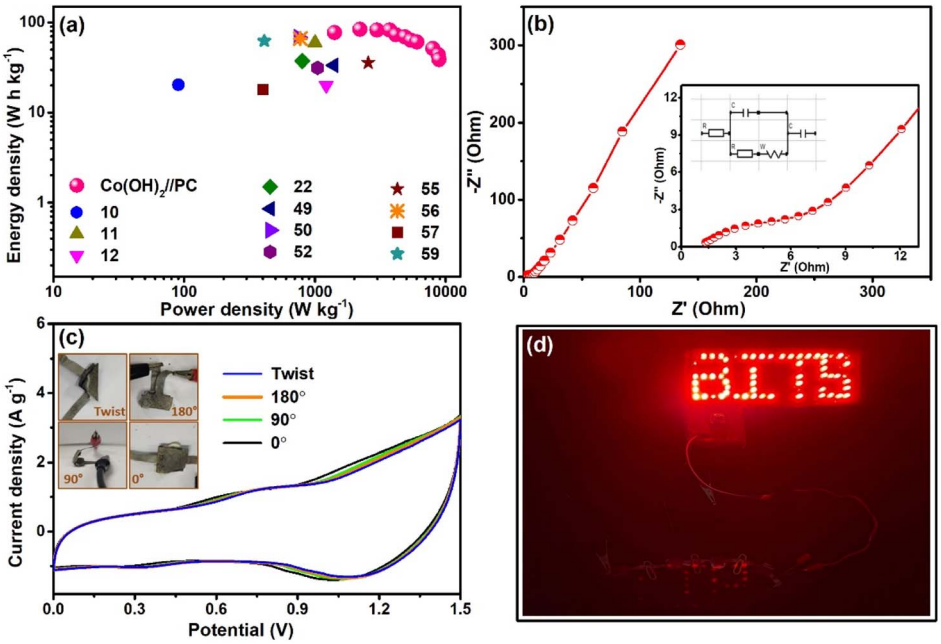

Fig. 7 (a) Ragone plot of the solid-state $Co(OH)_2$//PC ASC device with a comparison of reported research on $Co(OH)_2$-based supercapacitors, (b) Nyquist plot, and (c) CV test with different angles of the solid-state ASC device. (d) LED light illuminated by the solid-state ASC device.

The Ragone plot (Fig. 7a) was derived from the resultant energy and power density values and compared with a few of the values reported on $Co(OH)_2$ and/or porous carbon-based ASC devices. The energy density of the solid-state $Co(OH)_2$//PC device was found to be 76.7 W h kg^{-1} at a power density of 1416.9 W kg^{-1}. These resultant values were comparable and, in

Table 1 Comparison of the fabricated $Co(OH)_2$//PC ASC device (this work) with some of the already reported $Co(OH)_2$-based two-electrode supercapacitors

Sr. No.	Material	Electrolyte	Potential (V)	Energy density (W h kg^{-1})	Power density (W kg^{-1})	Retention (cycles)	Ref.
1	$Co(OH)_2$/GNS//AC/CFP	1 M KOH	1.5	19.3	187.5	109% (20 000)	44
2	Ni1–Co_2–S/$Co(OH)_2$//AC	PVA/KOH	1.6	48.8	800	88% (10 000)	45
3	$Co(OH)_2$@PPy//CNTMN	PVA/KOH	1.6	10.53@mW h cm^{-3}	0.53@W cm^{-3}	89% (5000)	46
4	$Co(OH)_2$ NAs@Ni//CNTs@Ni	2 M KOH	1.5	19.05	112.5	~96% (7000)	47
5	CF–$Ni(OH)_2$//CF–CNT	PVA–KOH	1.4	41.1	1400	98% (3000)	48
6	CF–$Co(OH)_xCO_3$//CF–CNT	PVA–KOH	1.4	33.45	1400	97.6% (3000)	49
7	MnS/Ni_3S_2@$Co(OH)_2$//AC	1 M KOH	1.5	68.6	750	91.2% (10 000)	50
8	A-ZCo@NF//AC@GF	3 M KOH	1.5	365.5@μW h cm^{-2}	752.5@μW cm^{-2}	80.86% (10 000)	14
9	$Co(OH)_2$/rGO//AC	PVA/KOH	1.4	28	1754	89% (4000)	20
10	ACH//ACH	2 M KOH	—	6.85	601.46	95% (5000)	51
11	$Co(OH)_2$//$Co(OH)_2$	1 M KOH	1.2	3.96	42 000	81% (5000)	21
12	AC//$Co(OH)_2$ buds/Ni foam	6 M KOH	1.6	20.3	90.6	69.3% (1000)	10
13	β-$Co(OH)_2$//AC	6 M KOH	1.6	37.3	800	>90% (5000)	22
14	β-$Co(OH)_2$//rGO	6 M KOH	1.4	20.05	1220	93% (10 000)	12
15	$Co(OH)_2$@PANI//AC	6 M KOH	1.4	31.2	1050	74.8% (5000)	52
16	$Co(OH)_2$/fCNT//fCNT	PVA : KOH	1.4	3.8	7000	84% (5000)	53
17	CF/Cu$(OH)_2$/$Co(OH)_2$//CF/AC	PVA–KOH	1.5	3.5@mW h cm^{-2}	1.87@mW cm^{-2}	81% (12 000)	54
18	$Co_2(CO_3)(OH)_2$NDs/NiCo$(CO_3)(OH)_2$//graphene	1 M KOH	—	35.5	2555.6	71.3% (10 000)	55
19	$MgCo_2O_4$@α-$Co(OH)_2$/NF-2//AC	PVA–KOH	1.6	65.94	773.19	91.7% (10 000)	56
20	AC//AC/MB-400/$Co(OH)_2$	3 M KOH	1.6	18	400	80.05% (5000)	57
21	Cu$(OH)_2$@ZnNi–CoCH//AC	PVA–KOH	1.5	34.75	375	86.54% (6000)	35
22	$Co(OH)_2$@$NiMoS_4$//AC	3 M KOH	2.0	59.5	1000	100% (5000)	11
23	β-$Co(OH)_2$//AC	6 M KOH	1.2	10	300	69.6% (5000)	23
24	Co_3O_4/$Co(OH)_2$//AC	2 M KOH	1.5	25.6	939	84.5% (5000)	58
25	Mn–$Co(OH)_2$/CoS//AC	2 M KOH	1.65	62.1	410	164.1% (30 000)	59
26	$Co(OH)_2$//PC	KOH + PVA	1.5	76.7	1416.9	91% (5000)	This work

a few cases, superior to the values found in the literature (Table 1). The R_S and R_{CT} values of the solid-state ASC were determined from EIS measurements (Nyquist plot and equivalent circuit as inset presented in Fig. 7b). R_S and R_{CT} values were 0.95 and 1.41 Ω, respectively. Equivalent circuit resistance (ESR) was calculated by summing R_S and R_{CT} values, The low value of ESR of this device contributes to its high power density.[8]

To establish the flexibility of the device, CV measurement was performed when bending it at different angles (Fig. 7c). Almost identical CV profiles were observed for the different bending shapes of this device, which illustrated its remarkable flexibility. The as-fabricated device effectively lit up a panel of red LEDs, which validated its real-life applicability (Fig. 7d).

4. Conclusions

In conclusion, the $Co(OH)_2$ hollow sphere was synthesized using a single-step hydrothermal process. Biomass-derived (*i.e.*, from the tea waste) porous carbon was synthesized using the KOH activation method, which showed a highly porous matrix. $Co(OH)_2$ showed redox activity in an alkaline medium with a high C_S value of 801 F g^{-1} at a current density of 1 A g^{-1}. Moreover, porous carbon exhibited an EDLC nature and C_S value of 516 F g^{-1} at a current density of 1 A g^{-1}. An asymmetric supercapacitor device was assembled using $Co(OH)_2$ as a cathode and PC as an anode. First, the filter paper soaked in KOH was used as an electrolyte/separator to test the ASC device, which verified its good activity as an ASC device. Then, a gel electrolyte with PVA and KOH was prepared to fabricate a flexible solid-state $Co(OH)_2$//PC ASC device. The prepared PVA + KOH gel electrolyte acted as an electrolyte and a separator. The solid-state $Co(OH)_2$//PC ASC device performed well and showed a high C_S value of 260 F g^{-1} at a current density of 2 A g^{-1}. It retained ∼91% of the initial C_S value (at 6 A g^{-1}) till ∼5000 cycles. The high-performance $Co(OH)_2$//PC ASC device exhibited an energy density of 76.7 W h kg^{-1} at a power density of 1416.9 W kg^{-1}. Thus, this study presents an improved performance of cobalt hydroxide and porous carbon for asymmetric supercapacitor devices.

Data availability

All relevant data are available from the corresponding authors upon reasonable request.

Author contributions

Rajeshvari Samatbhai Karmur and Debika Gogoi: conceptualization, investigation, validation, methodology, formal analysis, data curation, writing – original draft, writing – review & editing, visualization. Manash R. Das: XPS analysis data collection. Narendra Nath Ghosh: resources, funding acquisition, supervision, data curation, writing – review & editing.

Conflicts of interest

The authors disclose that they have no conflicting financial interests.

Acknowledgements

N. N. G. acknowledges the Cross-Disciplinary Research Framework (CDRF) scheme BITS Pilani, India (Grant: C1/23/121) for providing financial support. The R. S. K. is thankful to CSIR-HRDG, India, for awarding a senior research fellowship (File No. 09/0919(11330)/2021-EMR-I). The authors acknowledge the Central Sophisticated Instrumentation Facility (CSIF), BITS Pilani K. K. Birla Goa Campus, for providing Raman spectroscopy, FESEM, and EDX facilities.

References

1 A. Buylova, N. Nasiritousi, A. Duit, G. Reischl and P. Lejon, *Environ. Sci. Policy*, 2024, **159**, 103811.
2 C. Cruanyes, O. Alcaraz and B. Sureda, *Clim. Policy*, 2024, **24**, 691–705.
3 R. Morya, T. Raj, Y. Lee, A. Kumar Pandey, D. Kumar, R. Rani Singhania, S. Singh, J. Prakash Verma and S.-H. Kim, *Bioresour. Technol.*, 2022, **366**, 128159.
4 P. Makkar and N. N. Ghosh, *ACS Omega*, 2020, **5**, 10572–10580.
5 S. Natarajan, M. Ulaganathan and V. Aravindan, *J. Mater. Chem. A*, 2021, **9**, 15542–15585.
6 S. Sharma and P. Chand, *Results Chem.*, 2023, **5**, 100885.
7 S. A. Kadam, K. P. Kadam and N. R. Pradhan, *J. Mater. Chem. A*, 2024, **12**, 17992–18046.
8 Y. Shao, M. F. El-Kady, J. Sun, Y. Li, Q. Zhang, M. Zhu, H. Wang, B. Dunn and R. B. Kaner, *Chem. Rev.*, 2018, **118**, 9233–9280.
9 F. Wang, S. Xiao, Y. Hou, C. Hu, L. Liu and Y. Wu, *RSC Adv.*, 2013, **3**, 13059–13084.
10 U. M. Patil, S. C. Lee, J. S. Sohn, S. B. Kulkarni, K. V. Gurav, J. H. Kim, J. H. Kim, S. Lee and S. C. Jun, *Electrochim. Acta*, 2014, **129**, 334–342.
11 J. Li, J. Zhao, L. Qin, Q. Zhang, X. Tang and Y. Xu, *RSC Adv.*, 2020, **10**, 22606–22615.
12 M. Jana, P. Sivakumar, M. Kota, M. G. Jung and H. S. Park, *J. Power Sources*, 2019, **422**, 9–17.
13 L. Pan, D. Wang, J. Wang, Y. Chu, X. Li, W. Wang, N. Mitsuzaki, S. Jia and Z. Chen, *Phys. Chem. Chem. Phys.*, 2024, **26**, 9096–9111.
14 C. Jagtap, V. Kadam, B. Kamble, P. E. Lokhande, A. Pakdel, D. Kumar, R. Udayabhaskar, A. Vedpathak, N. B. Chaure and H. M. Pathan, *J. Energy Storage*, 2024, **83**, 110666.
15 A. S. Pillai, R. Rajagopalan, A. Amruthalakshmi, J. Joseph, A. Ajay, I. Shakir, S. V. Nair and A. Balakrishnan, *Colloids Surf., A*, 2015, **470**, 280–289.
16 M. Qorbani, N. Naseri and A. Z. Moshfegh, *ACS Appl. Mater. Interfaces*, 2015, **7**, 11172–11179.
17 O. C. Pore, A. V. Fulari, R. V. Shejwal, V. J. Fulari and G. M. Lohar, *Chem. Eng. J.*, 2021, **426**, 131544.
18 S. Alipoori, S. Mazinani, S. H. Aboutalebi and F. Sharif, *J. Energy Storage*, 2020, **27**, 101072.
19 B. Jinisha, K. M. Anilkumar, M. Manoj, C. M. Ashraf, V. S. Pradeep and S. Jayalekshmi, *J. Solid State Electrochem.*, 2019, **23**, 3343–3353.

20 C. P. Roshni, K. Jithesh, P. M. Anjana, K. G. Raj and R. B. Rakhi, *Next Mater.*, 2024, **4**, 100199.
21 A. D. Jagadale, V. S. Kumbhar, D. S. Dhawale and C. D. Lokhande, *Electrochim. Acta*, 2013, **98**, 32–38.
22 M. Ulaganathan, M. M. Maharjan, Q. Yan, V. Aravindan and S. Madhavi, *Chem.–Asian J.*, 2017, **12**, 2127–2133.
23 I. M. Babu, J. J. William and G. Muralidharan, *Ionics*, 2019, **25**, 2437–2444.
24 D. Gogoi, R. S. Karmur, M. R. Das and N. N. Ghosh, *Energy Fuels*, 2023, **37**, 14350–14364.
25 Z. Wang, S. Ji, F. Liu, H. Wang, X. Wang, Q. Wang, B. G. Pollet and R. Wang, *ACS Appl. Mater. Interfaces*, 2019, **11**, 29791–29798.
26 D. McAteer, I. J. Godwin, Z. Ling, A. Harvey, L. He, C. S. Boland, V. Vega-Mayoral, B. Szydłowska, A. A. Rovetta, C. Backes, J. B. Boland, X. Chen, M. E. G. Lyons and J. N. Coleman, *Adv. Energy Mater.*, 2018, **8**, 1702965.
27 J. Yang, H. Liu, W. N. Martens and R. L. Frost, *J. Phys. Chem. C*, 2010, **114**, 111–119.
28 C. Lai, *J. Alloys Compd.*, 2019, **777**, 492–498.
29 A.-A. Malek Barmi, M. Aghazadeh, B. Arhami, H. M. Shiri, A. A. Fazl and E. Jangju, *Chem. Phys. Lett.*, 2012, **541**, 65–69.
30 J. P. Cheng, L. Liu, J. Zhang, F. Liu and X. B. Zhang, *J. Electroanal. Chem.*, 2014, **722–723**, 23–31.
31 L. Liu, J. P. Cheng, J. Zhang, F. Liu and X. B. Zhang, *J. Alloys Compd.*, 2014, **615**, 868–874.
32 J. T. Mehrabad, M. Aghazadeh, M. G. Maragheh, M. R. Ganjali and P. Norouzi, *Mater. Lett.*, 2016, **184**, 223–226.
33 J. Li, Z. Li, F. Zhan and M. Shao, *Chem. Sci.*, 2021, **12**, 1756–1761.
34 Y. Kou, J. Liu, Y. Li, S. Qu, C. Ma, Z. Song, X. Han, Y. Deng, W. Hu and C. Zhong, *ACS Appl. Mater. Interfaces*, 2018, **10**, 796–805.
35 Y. Liu, X. Cao, L. Cui, Y. Zhong, R. Zheng, D. Wei, C. Barrow, J. M. Razal, W. Yang and J. Liu, *J. Power Sources*, 2019, **437**, 226897.
36 Y. Xu, Z. Liu, D. Chen, Y. Song and R. Wang, *Prog. Nat. Sci.: Mater. Int.*, 2017, **27**, 197–202.
37 D. Gogoi, R. S. Karmur, M. R. Das and N. N. Ghosh, *Sustainable Energy Fuels*, 2022, **6**, 3599–3610.
38 Z. Huang, Y. Zhao, Y. Song, Y. Zhao and J. Zhao, *Colloids Surf., A*, 2017, **516**, 106–114.
39 J. Wang and S. Kaskel, *J. Mater. Chem.*, 2012, **22**, 23710–23725.
40 L. Cao, F. Xu, Y. Y. Liang and H. L. Li, *Adv. Mater.*, 2004, **16**, 1853–1857.
41 J. Jiang, J. Liu, R. Ding, J. Zhu, Y. Li, A. Hu, X. Li and X. Huang, *ACS Appl. Mater. Interfaces*, 2011, **3**, 99–103.
42 J. Huang, Y. Xie, Y. You, J. Yuan, Q. Xu, H. Xie and Y. Chen, *Adv. Funct. Mater.*, 2023, **33**, 2213095.
43 N. O. Laschuk, E. B. Easton and O. V. Zenkina, *RSC Adv.*, 2021, **11**, 27925–27936.
44 C. Zhao, F. Ren, X. Xue, W. Zheng, X. Wang and L. Chang, *J. Electroanal. Chem.*, 2016, **782**, 98–102.
45 T. Xu, G. Li and L. Zhao, *Chem. Eng. J.*, 2018, **336**, 602–611.
46 J. S. Lee, D. H. Shin, W. Kim and J. Jang, *J. Mater. Chem. A*, 2016, **4**, 6603–6609.
47 T. Peng, H. Wang, H. Yi, Y. Jing, P. Sun and X. Wang, *Electrochim. Acta*, 2015, **176**, 77–85.
48 D. Ghosh, M. Mandal and C. K. Das, *Langmuir*, 2015, **31**, 7835–7843.
49 J. Yu, Z. Hou, H. Zhang and X. Zhou, *Fuel*, 2024, **357**, 129754.
50 X. Hu, Y. Xiao, X. Liu, C. Wang, P. Xu, T. Tan, H. Yue, Y. Xing and X. Liu, *Int. J. Hydrogen Energ*, 2024, **60**, 107–117.
51 S. Yang, K. Cheng, K. Ye, Y. Li, J. Qu, J. Yin, G. Wang and D. Cao, *J. Electroanal. Chem.*, 2015, **741**, 93–99.
52 A. Keshavarz, J. Tashkhourian and S. F. Nami-Ana, *J. Energy Storage*, 2023, **73**, 108825.
53 R. Ranjithkumar, S. E. Arasi, P. Devendran, N. Nallamuthu, A. Arivarasan, P. Lakshmanan, S. Sudhahar and M. K. Kumar, *Diamond Relat. Mater.*, 2020, **110**, 108120.
54 B. K. Satpathy, S. Patnaik and D. Pradhan, *ACS Appl. Energy Mater.*, 2022, **5**, 77–87.
55 D. Lee, Q. X. Xia, J. M. Yun and K. H. Kim, *Appl. Surf. Sci.*, 2018, **433**, 16–26.
56 Z. Liu, Y. Qiu, A. Zhang, W. Yang, C. J. Barrow, J. M. Razal, A. Li and J. Liu, *Appl. Surf. Sci.*, 2021, **568**, 150856.
57 C. Xu, Y. Chen, Y. Ma, J. Huang, J. Zhao and H. Xu, *Electrochim. Acta*, 2021, **367**, 137475.
58 J. Mei, W. Fu, Z. Zhang, X. Jiang, H. Bu, C. Jiang, E. Xie and W. Han, *Energy*, 2017, **139**, 1153–1158.
59 Z. Gan, X. Ren, Y. Sun, M. Sun, Y. Yan, B. Cao, W. Shen, H. Yu, Z. Li and Y. Fu, *J. Energy Storage*, 2023, **69**, 107934.